J. Fluid Mech. (2014), *vol.* 752, *pp.* 123–139. © Cambridge University Press 2014
doi:10.1017/jfm.2014.255

Explosions at the water surface

Adrien Benusiglio[1], David Quéré[2] and Christophe Clanet[1,†]

[1]Ladhyx, Unité Mixte de Recherche 7646, Centre National de la Recherche Scientifique-École Polytechnique, 91120 Palaiseau, France

[2]Physique et Mécanique des Milieux Hétérogènes, Unité Mixte de Recherche 7636, Centre National de la Recherche Scientifique-Paris 6-Paris 7-École Supérieure de Physique et de Chimie Industrielles, 75005 Paris, France

(Received 4 March 2013; revised 20 December 2013; accepted 5 May 2014; first published online 2 July 2014)

We study the shape and dynamics of cavities created by the explosion of firecrackers at the surface of a large pool of water. Without confinement, the explosion generates a hemispherical air cavity which grows, reaches a maximum size and collapses in a generic w-shape to form a final central jet. When a rigid open tube confines the firecracker, the explosion produces a cylindrical cavity that expands without ever escaping the free end of the tube. We discuss a potential flow model, which captures most of these features.

Key words: interfacial flows (free surface)

1. Introduction

The first studies on water entry cavities probably go back to the work of Worthington (Worthington & Cole 1900; Worthington 1908; Truscott, Brenden & Belden 2014). Cavities are classically produced by the impact of a solid (characteristic size R, velocity U_0, density ρ_s) on a liquid (viscosity η, density ρ, surface tension γ). The critical velocity at which a cavity appears depends on both the shape and wetting properties of the solid (Duez *et al.* 2007). The underlying applications include the impact of bullets (May 1952), torpedoes (May 1975), but also water walking lizards (Glasheen & McMahon 1996) and spiders: the diving *Argyroneta aquatica* entrains air with its body to build an underwater bell and survive (Seymour & Hetz 2011). The different types of cavities are classified in the phase diagram presented in figure 1, where the velocity is rescaled by $\eta/\rho R$ on the horizontal axis, and the size by the capillary length $a=\sqrt{\gamma/\rho g}$ on the vertical one.

This phase diagram defines four types of cavities. The ones corresponding to large spheres or torpedoes plunging at high speed into water form region A, where both Reynolds $\rho R U_0/\eta$ and Bond R/a numbers are large. These cavities are elongated in the direction of motion, and they pinch at half the distance from the interface after a characteristic time $\tau=\sqrt{R/g}$ independent of the velocity (Duclaux *et al.* 2007; Duez *et al.* 2007). The singularity at pinch-off was recently described in detail (Gekle *et al.* 2009; Gekle & Gordillo 2010; Gordillo & Gekle 2010). For smaller spheres

†Email address for correspondence: clanet@ladhyx.polytechnique.fr

https://doi.org/10.1017/jfm.2014.255 Published online by Cambridge University Press

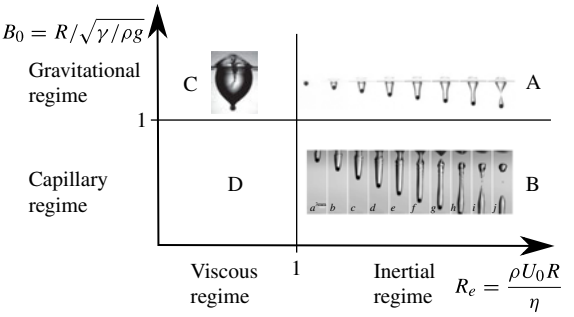


FIGURE 1. Phase diagram for entry cavities. In region A, B and C, pictures are taken from Duclaux *et al.* (2007), Aristoff & Bush (2009) and Le Goff, Quéré & Clanet (2013).

at high Reynolds number (region B), surface tension has a major role on the closure and produces wavy cavities (Aristoff *et al.* 2008; Aristoff & Bush 2009). If viscosity is increased (region C), we reach a regime where the sphere decelerates prior to closure (Le Goff *et al.* 2013). And we marginally expect cavities in the regime of low Reynolds and small Bond numbers. Apart from spheres, the impact of discs has also been studied (Bergmann *et al.* 2010), as well as non-axisymmetric objects (Enriquez *et al.* 2010, 2012).

In the present study, we inject energy into the fluid not by means of a directional impact, but with an explosion at the free surface, which generates an isotropic cavity at large Bond and Reynolds numbers. Results are presented in § 2, and confined explosions are studied in § 3.

2. Unconfined explosion cavities

2.1. *Set-up*

The set-up is sketched in figure 2(*a*): explosions are produced in a tank of polycarbonate (100 cm × 100 cm × 50 cm) filled with water ($\eta = 10^{-3}$ Pa s, $\gamma = 72 \times 10^{-3}$ N m^{-1}, $\rho = 10^3$ kg m^{-3}). We use four types of firecrackers (figure 2*b*) that contain 1, 1.3, 2 or 5 g of powder. The firecrackers are held vertically by a small wire and centred at the level of the free surface. Their characteristics are not altered as long as they do not stay more than 30 s in water. The explosion is recorded from the side with a high speed video camera (Photron Fastcam SA3) at 1000 frames s^{-1}. An acoustic measurement of the overpressure created by an explosion is shown in figure 2(*c*) where we observe that the explosion itself lasts less than 1 ms.

2.2. *Results*

Side views of the cavity created by the explosion of a 1 g firecracker are displayed in figure 3 as a function of time. For the first 4–5 ms (image 1 to image 2), the light produced by the explosion blinds the camera and we do not have access to this phase. Then, we observe that the explosion creates a hemispherical cavity, which expands radially up to 30 ms (images 1–5). Beyond this isotropic phase, the bottom of the cavity stops while the sides continue to expand. The cavity takes an elliptical shape (image 7). At this time ($T_{max} = 40$ ms), the bottom has reached its maximum depth $H_{max} = 50$ mm. In the collapsing phase, the bottom of the cavity accelerates backwards to the surface (images 8–18) with an eruption at the centre, making a

https://doi.org/10.1017/jfm.2014.255 Published online by Cambridge University Press

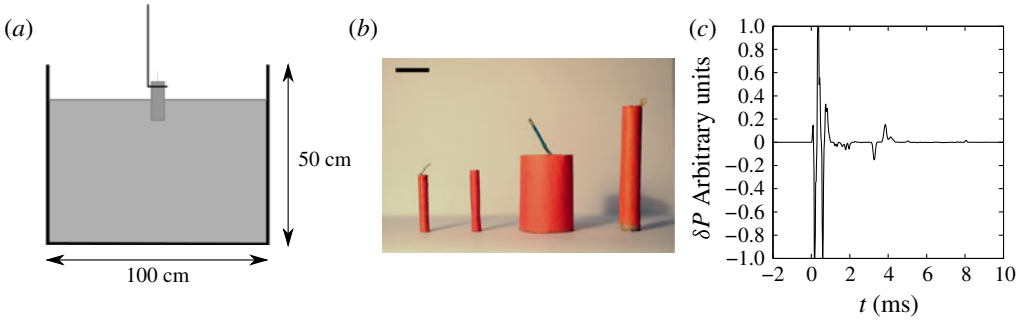


FIGURE 2. (Colour online) (*a*) Sketch of the experiment. (*b*) Four firecrackers containing 1, 1.3, 2 and 5 g of powder. The bar shows 2 cm. (*c*) Acoustic measurement of the overpressure produced by a 1 g firecracker explosion.

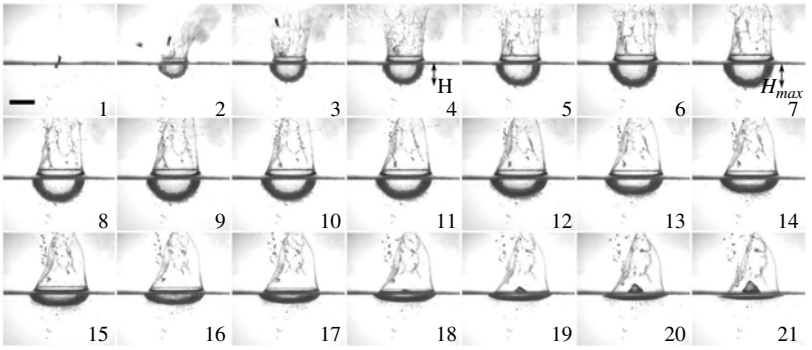


FIGURE 3. Chronophotography of the cavity created by the explosion of a 1 g firecracker. The video is taken from the side of the tank and we observe the evolution of the water/air interface. The time step between images is 7 ms. The bar in image 1 shows 5 cm. The depth of the cavity H reaches its maximum H_{max} at $t = T_{max}$ in image 7.

generic w-shaped cavity. The eruption is clearly visible at the end of the collapse, when the jet passes above the bath surface (images 19–21).

Quantitatively, we measure the time evolution of the depth H (defined in figure 3), and plot it in figure 4(*a*) for several explosions. The curves all have the same general shape: the velocity of expansion slows down until the cavity reaches its maximum depth H_{max} at a time T_{max}, which both seem to increase with the initial speed of expansion. The time T_{max} increases from 50 to 90 ms while the maximum depth varies from 40 to 170 mm. In a second phase ($t > T_{max}$), H decreases with an increasing velocity. The time evolution of H during these two phases presents a left–right symmetry with respect to T_{max}. In figure 4(*b*), we plot H as a function of time on a log-log graph for two cavities created by the explosion of 1 and 1.3 g firecrackers. We observe that, as time approaches zero, the function $H(t)$ tends toward a power law, $H = Kt^{\alpha}$, with $\alpha \approx 0.39 \pm 0.03$.

https://doi.org/10.1017/jfm.2014.255 Published online by Cambridge University Press

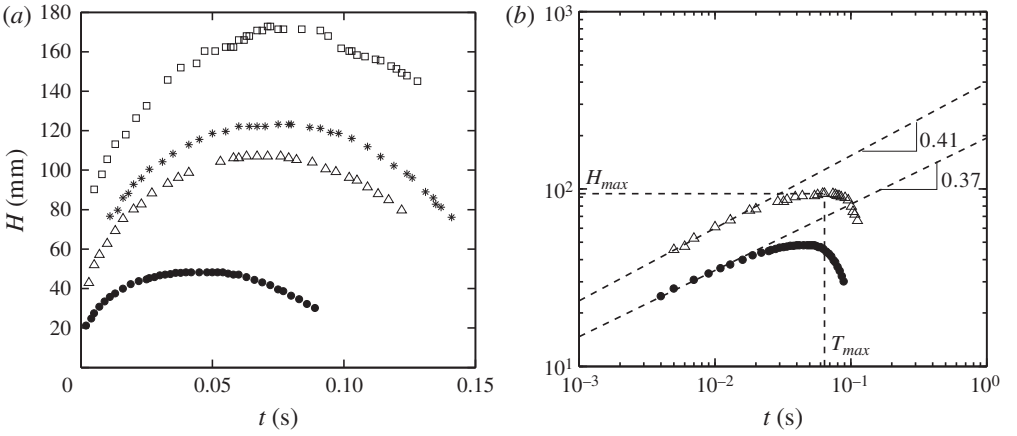


FIGURE 4. Depth of the cavity $H(t)$ during its expansion for explosions with a mass of powder of 1 g, '●'; 1.3 g, '△'; 2 g, '∗'; and 5 g, '□'. (*a*) Time evolution of the depth on a linear plot. (*b*) Time evolution of the depth on a log-log plot for the 1 and 1.3 g explosions.

2.3. *Modelling*

2.3.1. *Potential flow model*

The typical Reynolds number which characterizes the fluid motion during the cavity formation can be evaluated using the expansion time $T_{max} \approx 100$ ms needed to reach the maximum depth $H_{max} \approx 10$ cm (figure 3). This leads to $Re \approx \rho H_{max}^2/(T_{max}\eta) \approx 10^5$. Since the typical velocity is $H_{max}/T_{max} \approx 1$ m s^{-1}, the corresponding Mach number Ma is $H_{max}/(T_{max}c) \approx 10^{-3}$, $c = 1500$ m s^{-1} being the speed of sound in water. For high Reynolds number and small Mach number, viscous dissipation and compressibility can be neglected. Moreover, since the liquid is initially at rest, we use a potential flow approach to describe the cavity formation:

$$\left[\rho\frac{\partial\phi}{\partial t} + \frac{\rho u^2}{2} + p - \rho g z\right]_A^B = 0 \tag{2.1}$$

where ϕ is the velocity potential, $\boldsymbol{u} = \mathrm{grad}\,\phi$ the velocity of the water, g the acceleration of gravity, p the pressure, and A and B two points in water. The problem is sketched in figure 5: point A is chosen at the surface $[R_A = R(\theta)]$ and point B at the free surface, in an immobile region 'far' from the cavity. The radius $R(\theta, t)$ gives the interface location at time t in direction θ. We first assume that the explosion creates a brief overpressure, which isotropically puts the fluid into motion. The pressure then relaxes to ambient on a millisecond time-scale, shorter than the expansion time of the cavity which takes place over one hundred milliseconds (figure 4*b*). This is supported by the facts that the light flash (figure 3) lasts less than 5 ms, and overpressure (figure 2*b*) less than 1 ms. Hence we assume that the external pressure remains constant to ambient during the cavity expansion and collapse. Equation (2.1) thus becomes:

$$\rho\left.\frac{\partial\phi}{\partial t}\right|_A + \rho\frac{u_A^2}{2} - \rho g z_A - \gamma C_A = 0 \tag{2.2}$$

https://doi.org/10.1017/jfm.2014.255 Published online by Cambridge University Press

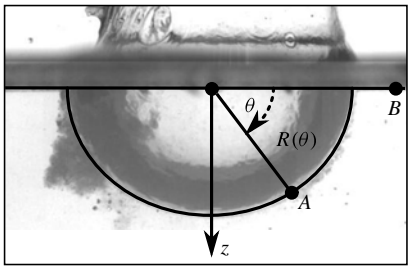


FIGURE 5. Sketch of the problem and notations used for the model.

where C_A is the mean curvature in A. Comparing the final two terms in (2.2) for a spherical cavity ($C_A = 2/R$), we deduce that gravity dominates capillary effects as soon as z_A becomes larger than $2a^2/R$, where $a = \sqrt{\gamma/(\rho g)}$ is the capillary length.

2.3.2. *A first evaluation of the potential* ϕ

Since the cavity is initially isotropic, the model is developed in the limit $\partial/\partial r \gg \partial/\partial\theta$ and $\partial/\partial\varphi = 0$, where φ stands for the azimuthal coordinate. In this limit, mass conservation implies $\partial(r^2 u_r)/\partial r = 0$, which yields $u_r = (R/r)^2\,\dot{R}$, from which we obtain the velocity potential $\phi(r,t) = -R^2\dot{R}/r$. The differential equation for the cavity dynamics follows from (2.2):

$$R\ddot{R} + \frac{3}{2}\dot{R}^2 = -gR\sin\theta - \frac{2\gamma}{\rho R}. \tag{2.3}$$

This equation can be integrated once:

$$\rho R^3\dot{R}^2 + \tfrac{1}{2}\rho g R^4 \sin\theta + 2\gamma R^2 = E_0 \tag{2.4}$$

where the constant of integration E_0 is the typical energy injected in the bath by the explosion. Equation (2.4) thus expresses the conversion of chemical energy into kinetic, gravitational and surface energies.

2.3.3. *Short time dynamics*

At short times, R is small (if the size of the firecracker is neglected in comparison to the size of the cavity, $R(t=0) = 0$), and (2.4) reduces to $R^3\dot{R}^2 = E_0/\rho$, which does not depend on θ. The expansion is isotropic, the cavity has an hemispherical shape (which justifies the expression of the curvature $C_A = 2/R$ used in (2.3)) and it expands following the law $R(t) = \left(5/2\sqrt{E_0/\rho}\right)^{2/5} t^{2/5}$. A similar power law was derived by Taylor for the luminous globe created by the explosion of an atomic bomb (Taylor 1950). Comparing this law with our experimental data (figure 4*b*) enables us to evaluate E_0 for each experiment. The typical values for E_0 lie between 0.2 and 15 J, and E_0 increases with the mass of powder in the firecracker.

As time proceeds, $\dot{R}(\theta)$ decreases down to the point where the second term in (2.4) dominates the first term. This term depends on θ, which introduces anisotropy into the cavity shape. It is maximum at the bottom ($\theta = \pi/2$) and vanishes on the sides ($\theta = 0$ and $\theta = \pi$). This implies that the bottom expansion slows down faster than the sides and that the acceleration during collapse is greater at the bottom. These features are consistent with the observations in figure 3.

https://doi.org/10.1017/jfm.2014.255 Published online by Cambridge University Press

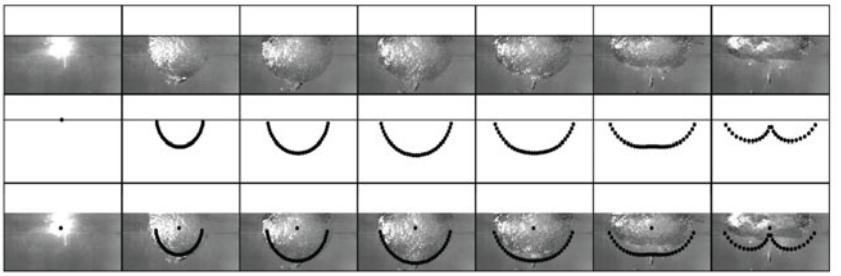


FIGURE 6. Comparison of the experimental shape of the cavity and the numerical solution of (2.4). The chronophotography corresponds to an explosion of a 1.3 g firecracker, with a time step of 22 ms. The maximum depth of the cavity is 10 cm. The numbers at the bottom of each column indicate the value of the ratio H/H_{max}.

One also notices in (2.4) that $\dot{R}$ only depends on R and θ. This means that for a given angle θ, during opening and collapse of the cavity, the absolute value of velocity $|\dot{R}|$ will be equal when the radius reaches a given value R. Hence we can understand why the curves $R(t)$ are symmetrical with respect to $t = T_{max}$, as observed in figure 4(*b*).

2.3.4. *Shape of the cavity*

We numerically solve (2.4) for several angles, and compare the resulting profiles to a typical experiment in figure 6. The numerical solution correctly captures the time evolution of the cavity, with an isotropic expansion followed by a flattening of the bottom and finally a focusing of the flow at this place. When focusing occurs, the flow is no longer radial and a vertical jet appears, which regularizes the cusp. The same behaviour was already seen in a model proposed by Daer, Field & Walton (1988) for the problem of cavity collapse by a shock wave, and also in the context of Munroe jets (Bowden 1966).

Setting $\dot{R}(H_{max}) = 0$ in (2.4), we obtain a relationship between E_0 and the maximum depth of the cavity $H_{max} = R_{max}(\pi/2)$:

$$H_{max} = \left(\frac{2E_0}{\rho g}\right)^{1/4}. \tag{2.5}$$

We can then check (2.5) by plotting the measured maximum depth, H_{max}, as a function of the distance $(2E_0/(\rho g))^{1/4}$. We observe in figure 7 that H_{max} indeed linearly varies with $(2E_0/(\rho g))^{1/4}$ (with a constant of proportionality close to unity), in agreement with (2.5).

2.3.5. *Rescaling and dynamics*

It follows from the model that natural scales for H and t are, respectively, $H_{max} \equiv \max[R(\theta = \pi/2)]$ and $\tau = \sqrt{H_{max}/g}$. Letting $\bar{H} = H/H_{max}$ and $\bar{t} = t/\tau$ denote the corresponding dimensionless variables, we can check that the series of data collapse on a master curve when plotting $\bar{H}$ as a function of $\bar{t}$ (figure 8). The evolution equation of the cavity can be written in terms of these scaled variables:

$$\dot{\bar{R}} = \pm\sqrt{\frac{1 - \bar{R}^4 \sin\theta + 4\,(a/H_{max})^2\,(1 - \bar{R})}{2\bar{R}^3}} \tag{2.6}$$

https://doi.org/10.1017/jfm.2014.255 Published online by Cambridge University Press

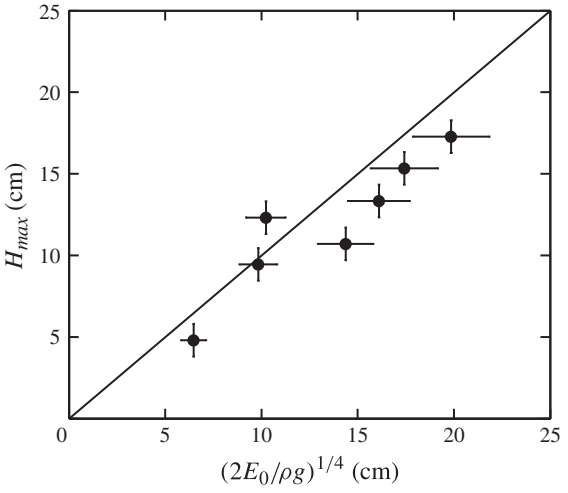


FIGURE 7. Maximum depth of the cavity as a function of the initial energy injected by the explosion. The solid line represents the linear relation expected from (2.5).

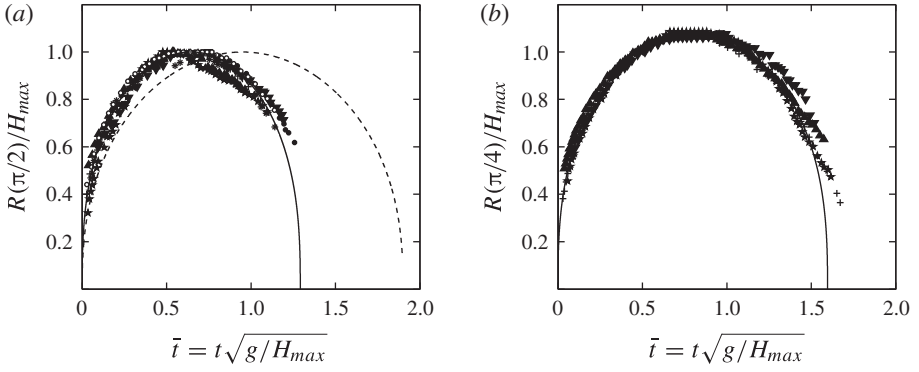


FIGURE 8. (*a*) Dimensionless depth of the cavity for several explosions as a function of dimensionless time. Symbols: '○', 1 g firecracker; '+, ∗', 1.3 g firecracker; '△, ∇, ⋆', 2 g firecracker; '●', 5 g firecracker. The numerical solution of (2.6) is drawn with a dashed line. The numerical solution of a modified equation (2.13) described in § 2.4 is plotted with a solid line. (*b*) Dimensionless position of the surface at the angle $\pi/4$ as a function of dimensionless time. The black curve is the numerical solution of (2.13).

where the plus and minus signs correspond to expansion and contraction, respectively. The solution of (2.6) is drawn with a dashed line in figure 8 and compared to experiment. Even if the general shape is satisfactory, (2.6) does not precisely describe the observed dynamics, so the model must be refined.

2.4. *Refined model*

The above model does not describe the corolla. In other words, there is some tangential velocity in the flow field, which results from the explosion and which has not been accounted for. It is the purpose of this section to discuss this effect and complete the model. To quantify this tangential velocity, we took long time exposure

https://doi.org/10.1017/jfm.2014.255 Published online by Cambridge University Press

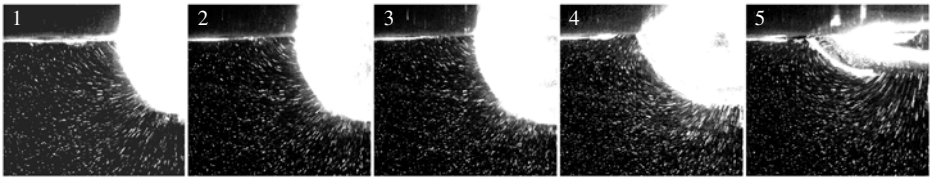


FIGURE 9. Flow after the explosion of a 1 g firecracker. Stream lines are obtained by superimposing images, water being seeded with particles and illuminated with a vertical laser light sheet. Images 1, 2 and 3 show the stream lines during opening of the cavity; images 4 and 5 during closure.

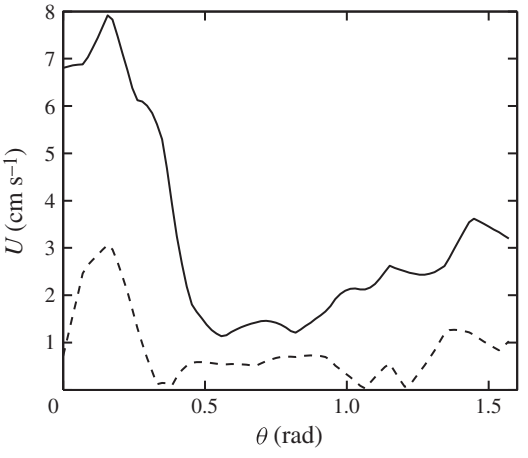


FIGURE 10. Evolution of the radial velocity (solid line) and tangential velocity (dashed line) close to the cavity surface at approximately one half of the opening phase, as a function of the angle θ. The data correspond to the explosion of figure 9.

pictures, as shown in figure 9. The tangential component is clearly visible in the region close to the interface. Images are treated with Matlab to obtain the velocity field, using a code developed by Meunier and Leweke (Meunier & Leweke 2003, 2005), and the radial and tangential values of the velocity are compared in figure 10. This comparison reveals that the tangential component is small compared to the radial component. Since our main goal here is to describe the shape and dynamics of the cavity and not to have a precise description of the flow, we account for this perturbation of the radial flow by modifying the expression of the radial component of the velocity:

$$u_r = \alpha \frac{R^2}{r^2} \dot{R}. \tag{2.7}$$

In this expression, α is a constant, the value of which lies between zero and one. If all the displacement of the surface leads to the ejection of water in the liquid sheet, α is equal to zero; if there is no flow ejected upwards, we have $\alpha = 1$. The potential of the flow thus becomes $\phi(r, t) = -\alpha R^2 \dot{R}/r$. The equation of motion of the cavity is:

$$\alpha R \ddot{R} + \alpha(2 - \alpha/2)\dot{R}^2 = -gR \sin\theta - \frac{2\gamma}{R}. \tag{2.8}$$

https://doi.org/10.1017/jfm.2014.255 Published online by Cambridge University Press

Its primary integral is:

$$\rho R^{4-\alpha}\dot{R}^2 + \frac{2\rho g \sin\theta}{\alpha(5-\alpha)}R^{5-\alpha} + \frac{4\gamma}{\alpha\,(3-\alpha)}R^{3-\alpha} = K_0. \tag{2.9}$$

For $\alpha = 1$, this equation reduces to (2.4). In order to close the problem, an argument is needed to evaluate α. This is done by studying the acceleration field when the cavity has reached its maximal extension.

2.4.1. *Why* $\alpha = 1/2$*?*

The argument developed in this subsection is due to Dr Mark Cooker. (Mark Cooker is Senior Lecturer in the School of Mathematics at the University of East Anglia in Norwich. We discussed this problem at the ICMF conference in Edinburgh organized by Alexander Korobkin in 2013 on the 'Mathematics of Splashing'.) At the maximal extension (image 7 in figure 3), the velocity vanishes (the cavity stops) while the acceleration is maximal. At this special moment, the equation of motion reduces to $[\rho\partial\phi/\partial t + p - \rho g z]_A^B = 0$. Taking the Laplacian of this equation leads to $\Delta p = 0$. Assuming that the cavity is almost spherical due to an isotropic expansion, the solution to this harmonic equation is:

$$p(r,\theta) = p_0 - \frac{2\gamma}{R} + \rho g r\sin\theta\left[1 - \left(\frac{R}{r}\right)^3\right]. \tag{2.10}$$

This pressure field makes it possible to calculate the acceleration field at the maximal extension: $\partial \boldsymbol{U}/\partial t = \mathrm{grad}(\partial\phi/\partial t)$. Since we have $\partial\phi/\partial t = g\sin\theta R^3/r^2$, we get:

$$\frac{\partial \boldsymbol{U}}{\partial t} = -2g\sin\theta\frac{R^3}{r^3}\boldsymbol{e}_r + g\cos\theta\frac{R^3}{r^3}\boldsymbol{e}_\theta. \tag{2.11}$$

At $\theta = \pi/2$, the acceleration of the cavity is directed upward and its value is $2g$! This value of the acceleration is effectively measured in the experiments and can be used to fix α. According to (2.8), the acceleration $\ddot{R}$ when $\dot{R} = 0$ satisfies $\alpha R\ddot{R} = -gR\sin\theta - 2\gamma/R$. For $\theta = \pi/2$ the capillary effect is negligible (the cavity is much larger than the capillary length) and the acceleration reduces to $\ddot{R} = -g/\alpha$. Thus $\alpha = 1/2$ enables us to recover the value deduced from the analysis of the pressure field at the maximal extension.

2.4.2. *Impact of the new model on the dynamics*

With $\alpha = 1/2$, (2.9) can be written:

$$R^{7/2}\dot{R}^2 + \frac{8}{9}g\sin\theta R^{9/2} + \frac{16}{5}\frac{\gamma}{\rho}R^{5/2} = \frac{8}{9}g\sin\theta H_{max}^{9/2} + \frac{16}{5}\frac{\gamma}{\rho}H_{max}^{5/2}. \tag{2.12}$$

We deduce the relationship between the velocity of the interface and its location:

$$\bar{\dot{R}} = \pm\sqrt{\frac{8}{9}}\sqrt{\frac{1 - \bar{R}^{9/2}\sin\theta + 18/5\,(a/H_{max})^2\left(1-\bar{R}^{5/2}\right)}{\bar{R}^{7/2}}}. \tag{2.13}$$

The numerical solution of this equation is drawn with a solid line in figure 8 for two different values of the angle: $\theta = \pi/2$ in figure 8(*a*) and $\theta = \pi/4$ in figure 8(*b*). In both cases, the dynamics predicted by (2.13) is in close agreement with experiment.

https://doi.org/10.1017/jfm.2014.255 Published online by Cambridge University Press

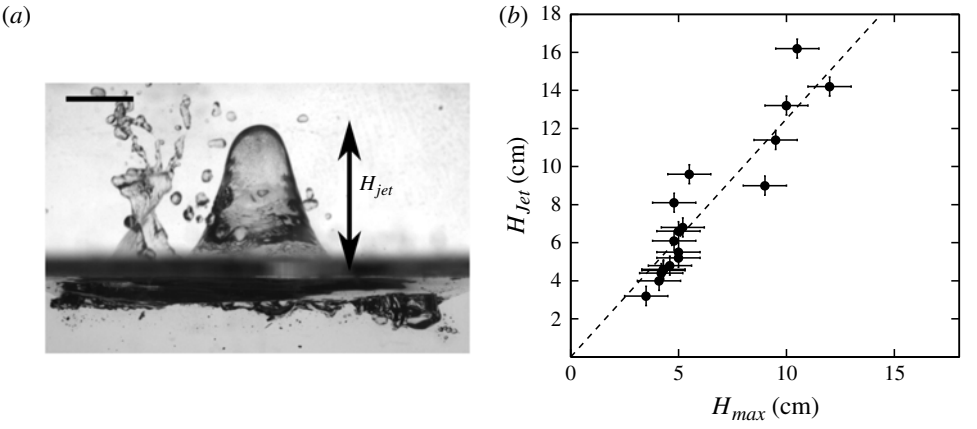


FIGURE 11. (*a*) Eruption created by the cavity of a 5 g firecracker explosion. The bar shows 3 cm. (*b*) Height of the jet as a function of the cavity depth. The best linear fit is shown in dashed line.

2.4.3. *Short time dynamics*

In the limit $\bar{R} \ll 1$, (2.13) reduces to $\bar{R}^{7/4}\dot{\bar{R}} = \sqrt{8/9}$, which leads to the dynamics:

$$\bar{R} = \sqrt{\tfrac{121}{18}}\bar{t}^{4/11}. \tag{2.14}$$

This $t^{4/11}$ behaviour hardly differs from $t^{2/5}$ and it remains compatible with the experiments in figure 4(*b*).

2.5. *Side effects*

In this section we qualitatively discuss side effects, namely the formation of a jet during closure and the presence of ripples on the cavity surface.

2.5.1. *The resulting jet*

A close view of a jet formed during cavity closure is shown in figure 11(*a*). These jets reach a maximal height H_{Jet} proportional to the maximum depth of the cavity H_{max} (figure 11*b*). The jet width is comparable to its height. This eruption largely differs from Worthington jets observed after impact and cavity pinch-off, or after acceleration of a curved surface (Antkowiak *et al.* 2007), large bubble rupture in viscous fluid (Séon & Antkowiak 2012) or cavitation (Peters *et al.* 2013), for which jets are much thinner and faster, possibly even supersonic (Tagawa *et al.* 2012). In our problem, the cavity dimension is much larger and the collapse is gravity-driven, which induces a much weaker focusing of the flow.

2.5.2. *Ripples*

Zooming on the cavity surface during expansion reveals millimetric ripples that become centimetric as the cavity grows (figure 12). We interpret these structures as arising from an initial Rayleigh–Taylor instability. During the explosion (1 ms long), the interface is accelerated towards the dense fluid (water), which triggers the instability. The characteristic initial speed of the cavity after explosion is 1 m s^{-1}, so

https://doi.org/10.1017/jfm.2014.255 Published online by Cambridge University Press

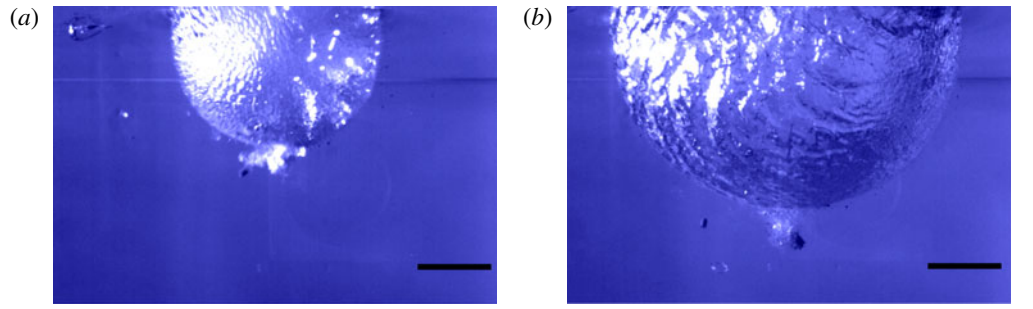


FIGURE 12. (Colour online) Surface of the water/air interface of the cavity during the initial growing phase ($t = T_{max}/2$ in a) and at maximum expansion ($t = T_{max}$ in b), after the explosion of a 2 g firecracker. The black segment shows 5 cm.

that the acceleration G during explosion is of the order of 250 m s^{-2}. The typical unstable wavelength for this acceleration is $\lambda \approx 2\pi\sqrt{\gamma/(\rho G)} \approx 3$ mm, comparable to the wavelength observed in figure 12. After the explosion, the expansion velocity decreases and the interface accelerates towards the light fluid (air), a stable situation with respect to Rayleigh–Taylor instability. This explains why the ripples do not grow in amplitude during expansion, but just get geometrically dilated.

3. Confined explosion cavities

We also conducted experiments where explosions were confined inside a vertical tube open at both ends, which forces cavities to expand in an anisotropic way.

3.1. *Set-up*

We use the same firecrackers as previously, and they similarly explode with their centre at the free surface. The confinement tubes are made of glass or polycarbonate, with diameters of 2, 4 or 5 cm and an immersed length L varying from 10 to 35 cm. The tubes are rigid and we never visualize any deformation at their surface.

3.2. *Results*

Two examples of confined explosions are presented in figures 13 and 14, with different explosion energies. Contrasting with unconfined geometries (where $R(t) \sim t^{0.39}$), the explosion of the firecracker first empties the tube at a constant velocity $\dot{Z}_0$ (images 1–4 in figure 13). This velocity depends on the mass and position of the firecracker, and on the mass of water to be put into motion.

In the first case (figure 13), the position Z of the air/water interface increases up to a maximum Z_{max} (images 1–12). The cavity then accelerates backward and closes (images 13–24). Later, the surface oscillates around the equilibrium height $Z = 0$ with a decreasing amplitude (Lorenceau *et al.* 2002). In the second case (figure 14), the cavity quickly grows and reaches the bottom end $Z = L$ (images 1–5 in figure 14). It then retracts without coming out of the tube. The dynamics $Z(t)$ for those two cavities are plotted in figure 15(a). The time evolution of Z is not symmetrical with respect to the moment T_{max} of maximal expansion. Rather, we observe that the velocity during closure is smaller than during expansion.

https://doi.org/10.1017/jfm.2014.255 Published online by Cambridge University Press

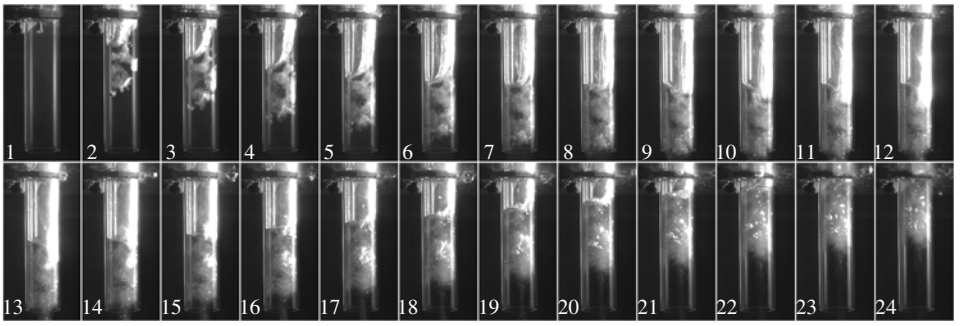


FIGURE 13. Chronophotography of a cavity created with a 5 g firecracker and confined in a tube of 5 cm diameter and 18.5 cm length. The initial velocity of expansion of the cavity is 1.3 m s^{-1}. The time step between images is 15 ms.

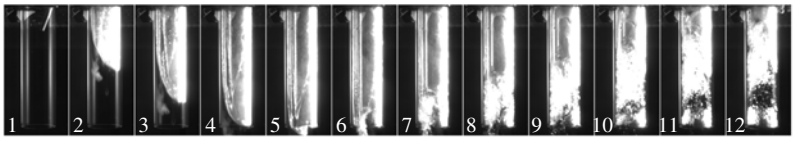


FIGURE 14. Chronophotography of a cavity created with a 5 g firecracker and confined in a tube of 5 cm in diameter and 17.3 cm in length. The initial velocity of expansion of the cavity is 3.3 m s^{-1}. The expansion stops at the end of the tube. The time step between images is 15 ms.

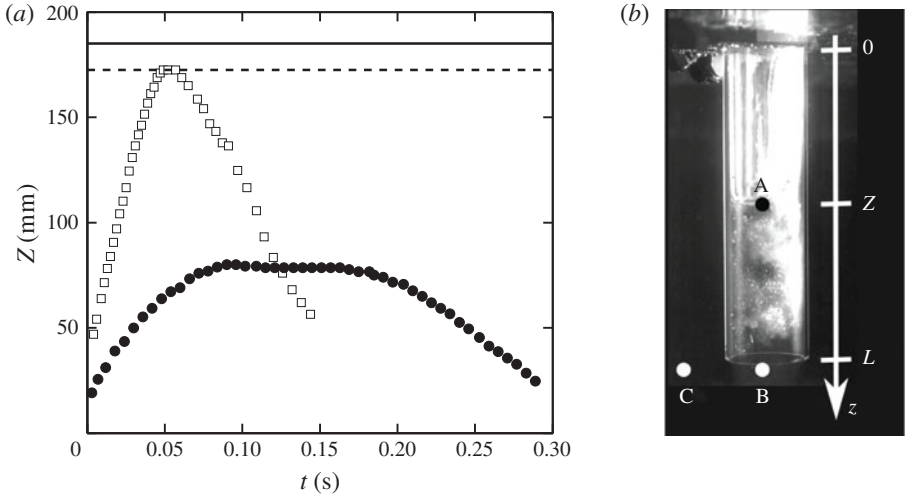


FIGURE 15. (*a*) Size of the cavity as a function of time for the two explosions of figures 13 and 14. In open squares, the cavity reaches the bottom end of the tube ($L = 173$ mm indicated with a dashed line) but does not exit ($Z \leqslant L$). In dots, the cavity stops far away from the end of the tube ($L = 185$ mm indicated with a solid line). (*b*) Sketch of the experiment and conventions used for the model.

https://doi.org/10.1017/jfm.2014.255 Published online by Cambridge University Press

3.3. *Modelling*

We model the problem as sketched in figure 15(*b*). The Reynolds number of the flow can be estimated from figure 13: the cavity expands to 75 mm in $T_{max} = 500$ ms in a 5 cm diameter tube, which yields $R_e = \rho D Z_{max}/T_{max}\eta = 7500$. Since the typical velocity ($\dot{Z}_0 \approx 1$ m s^{-1} in figure 15*a*) is small compared to the speed of sound, the flow can be treated as incompressible. Moreover, its initial state at rest suggests applying the potential flow approach again. Using the conventions of figure 15(*b*), we get

$$\left[\rho\frac{\partial\phi}{\partial t} + \frac{\rho u^2}{2} + p - \rho g z\right]_A^B = 0. \tag{3.1}$$

According to figure 15(*a*), the phenomenon typically lasts 100 ms. This implies that the boundary layer develops over a distance $\sqrt{\nu t}$ of the order of 0.1 mm (Lorenceau *et al.* 2002). We thus ignore the boundary layer and assume a plug-flow

$$\phi(z, t) = \dot{Z}(t) z. \tag{3.2}$$

At large Reynolds numbers, the streamlines of the outgoing jet remain almost parallel at the exit of the tube. This leads us to neglect the radial pressure gradient and to assume that the pressure in B is close to $P_0 + \rho g L$. Equation (3.1) then reduces to

$$(L - Z)\ddot{Z} = -gZ. \tag{3.3}$$

For the up-going phase, the end of the tube appears as a sink and we show in appendix A that the equation of motion can be written in the form

$$(L - Z)\ddot{Z} = -gZ + \dot{Z}^2/32. \tag{3.4}$$

We note that the equations for expansion (3.3) and closure (3.4) differ, in agreement with the observation made in figure 15(*a*). Since the up-going phase and subsequent oscillations are treated in Lorenceau *et al.* (2002), we focus below on the down-going phase.

3.4. *The low velocity limit*

In the low velocity limit $Z_{max} \ll L$, (3.3) reduces to that of an oscillator:

$$\ddot{Z} + \frac{g}{L}Z = 0, \tag{3.5}$$

the solution of which is

$$Z = Z_{max}\sin(\omega t) \tag{3.6}$$

with $\omega = \sqrt{g/L}$. Since $\dot{Z}(t=0) = \dot{Z}_0$, we get the relation $Z_{max} = \dot{Z}_0\sqrt{L/g}$. If we rewrite this equation in a dimensionless form, we obtain

$$\bar{Z}_{max} = \frac{Z_{max}}{L} = \frac{\dot{Z}_0}{\sqrt{gL}} = \sqrt{Fr} \tag{3.7}$$

where Fr is the Froude number. Hence, for cavities with 'small' initial velocity (small Froude number), the maximum depth linearly increases with the initial speed. In figure 17, we plot the maximum depth $\bar{Z}_{max}$ as a function of the Froude number. The experiments correspond to cavities obtained in tubes of length L varying between 10 and 35 cm. The initial speed $\dot{Z}_0$ is estimated from the best linear fit of $Z(t)$ during the first steps of expansion. The linear relation for small initial velocities is plotted with a dashed line. Only the data with Fr smaller than unity follow a linear relationship. Most of the experiments are outside this regime, and the cavity length is surprisingly found to saturate at the tube length, even at large Fr (up to five in these experiments). We now discuss this second regime.

https://doi.org/10.1017/jfm.2014.255 Published online by Cambridge University Press

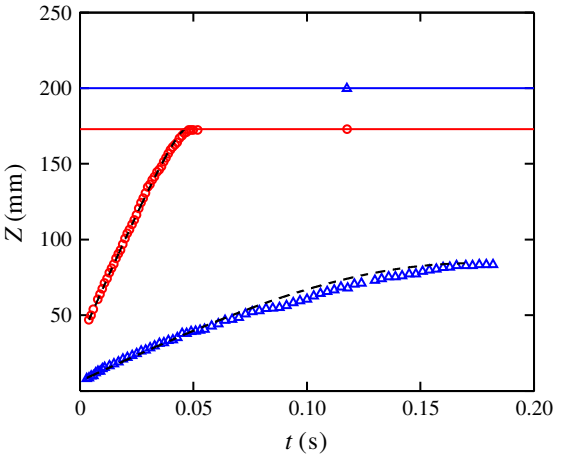


FIGURE 16. (Colour online) Depth as a function of time for two confined cavities, the one (red circles) expanding to the end of the tube indicated by a horizontal line ($Fr = 6.7$), and the other (blue triangles) of smaller expansion ($Fr = 0.24$). The numerical integration of (3.10) is drawn with a dashed line.

3.5. *The large velocity limit*

Using L and $\tau = \sqrt{L/g}$ to rescale length and time, (3.3) takes the form

$$(1 - \bar{Z})\ddot{\bar{Z}} = -\bar{Z}. \tag{3.8}$$

That equation can be rewritten:

$$\frac{1}{2}\frac{d\dot{\bar{Z}}^2}{d\bar{Z}} = \frac{-\bar{Z}}{1 - \bar{Z}}. \tag{3.9}$$

A primary integral of this equation is

$$\frac{\dot{\bar{Z}}^2}{2} = \frac{Fr}{2} + \bar{Z} + \ln(1 - \bar{Z}). \tag{3.10}$$

In figure 16 we compare the numerical integration of (3.10) with the experimental dynamics for two cavities, one with a small Froude number (in blue) and one with a large one (in red). In both cases, the model captures most of the experimental features.

Equation (3.10) also provides the maximum expansion $\bar{Z}_{max}$ of the cavity reached when $\dot{\bar{Z}} = 0$.

$$\frac{Fr}{2} = -\bar{Z}_{max} - \ln(1 - \bar{Z}_{max}). \tag{3.11}$$

This equation is drawn with a solid line in figure 17 where it is found to describe the experimental evolution up to saturation.

3.6. *The very large velocity limit*

In the limit $Fr \gg 1$, (3.11) leads to $\bar{Z}_{max} \approx 1 - \exp(-Fr/2)$ which asymptotically approaches unity, without reaching it (in agreement with figure 14): the cavity

https://doi.org/10.1017/jfm.2014.255 Published online by Cambridge University Press

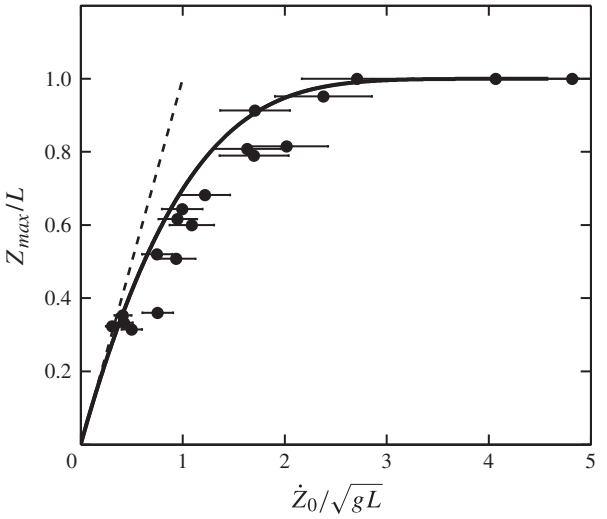


FIGURE 17. Dimensionless maximum cavity size as a function of the dimensionless initial velocity of the liquid in the tube after the explosion (dots). Equation (3.11) is drawn with a solid line, and its linear asymptote (3.7) with a dashed line.

remains confined in the tube (saturation regime in figure 17). This can be understood as follows: During explosion, the fluid in the tube is put into motion and then moves toward the bottom because of its inertia: in the meantime, it is subjected to a constant resisting force, F, induced by the hydrostatic pressure at the end of the tube ($F \sim \rho g L S$, where S is the cross-section of the tube). This constant force applies on a system of decreasing mass. In the large Froude number limit, the mass of liquid in the tube, m, vanishes and the constant force is able to decelerate it to rest, whatever its initial velocity (deceleration $\sim F/m$).

4. Conclusion

We studied the shape and dynamics of cavities created by the explosion of firecrackers at the surface of a large water pool. Without confinement, the cavity is hemispherical during its expansion, reaches the maximum depth H_{max} and then retracts in an anisotropic way. The maximum depth H_{max} is related to the energy E_0 of explosion via the relation $H_{max} \sim (E_0/(\rho g))^{1/4}$. The cavity opens and closes with a characteristic time $\sqrt{H_{max}/g} \sim 100$ ms, and its dynamics can be approached with a potential flow model.

When the explosion is confined within a tube open at both ends and immersed to a depth L, the cavity develops down to a depth Z_{max} whose value only depends on the Froude number based on the initial velocity $\dot{Z}_0$ ($Fr = \dot{Z}_0/\sqrt{gL}$). At small Froude number, the size of the cavity increases linearly with the velocity. At large Froude number it saturates to L: the cavity never goes out of the tube, whatever its initial speed.

Appendix A. The up-going phase of the confined cavity

During the up-going phase of the confined cavity, the flow at the exit of the tube is close to a sink flow. We write the flow potential in the bath $\phi_s = (-Q/(4\pi r))$ with

https://doi.org/10.1017/jfm.2014.255 Published online by Cambridge University Press

r the distance from the end of the tube. Since we have $Q = \dot{Z}\pi(D/2)^2$ (D being the tube diameter), we find

$$\phi_s = \frac{\dot{Z}R^2}{4r}. \tag{A 1}$$

We use the generalized Bernoulli equation to find the pressure at the bottom of the tube:

$$p_B = p_0 + \rho g L - \rho\frac{\dot{Z}^2}{32}. \tag{A 2}$$

Compared to the down going phase, where $p_B = p_0 + \rho g L$, the pressure difference applied to the liquid contained in the tube is smaller and one expects slower dynamics. More precisely, the dynamics is obtained via (3.1) and it takes the form

$$(L - Z)\ddot{Z} = -gZ + \frac{\dot{Z}^2}{32}. \tag{A 3}$$

REFERENCES

ANTKOWIAK, A., BREMOND, N., LE DIZÈS, S. & VILLERMAUX, E. 2007 Short-term dynamics of a density interface following an impact. *J. Fluid Mech.* **577**, 241–250.

ARISTOFF, J. M. & BUSH, J. W. M. 2009 Water entry of small hydrophobic spheres. *J. Fluid Mech.* **619**, 45–78.

ARISTOFF, J. M., TRUSCOTT, T. T., TECHET, A. H. & BUSH, J. W. M. 2008 The water-entry cavity formed by low bond number impacts. *Phys. Fluids* **20**, 091111.

BERGMANN, R., VAN DER MEER, D., GEKLE, S., VAN DER BOS, A. & LOHSE, D. 2010 Controlled impact of a disk on a water surface: cavity dynamics. *J. Fluid Mech.* **633**, 381–409.

BOWDEN, F. P. 1966 The formation of microjets in liquids under the influence of impact or shock. *Phil. Trans. R. Soc. Lond.* A **260**, 94–95.

DAER, J. P., FIELD, J. E. & WALTON, A. J. 1988 Gas compression and jet formation in cavities collapsed by a shock wave. *Nature* **332**, 505–508.

DUCLAUX, V., CAILLÉ, F., DUEZ, C., YBERT, C., BOCQUET, L. & CLANET, C. 2007 Dynamics of transient cavities. *J. Fluid Mech.* **591**, 1–19.

DUEZ, C., YBERT, C., CLANET, C. & BOCQUET, L. 2007 Making a splash with water repellency. *Nat. Phys.* **3**, 180–183.

ENRIQUEZ, O. R., PETERS, I. R., GEKLE, S., SCHMIDT, L. E., LOHSE, D. & VAN DER MEER, D. 2012 Collapse and pinch-off of a non-axisymmetric impact-created air cavity in water. *J. Fluid Mech.* **701**, 40–58.

ENRIQUEZ, O. R., PETERS, I. R., GEKLE, S., SCHMIDT, L. E., VERSLUIS, M., VAN DER MEER, D. & LOHSE, D. 2010 Collapse of nonaxisymmetric cavities. *Phys. Fluids* **22**, 091104.

GEKLE, S. & GORDILLO, J. M. 2010 Generation and breakup of Worthington jets after cavity collapse. Part 1. Jet formation. *J. Fluid Mech.* **663**, 293–330.

GEKLE, S., GORDILLO, J. M., VAN DER MEER, D. & LOHSE, D. 2009 High-speed jet formation after solid object impact. *Phys. Rev. Lett.* **102**, 034502-1, 034502-4.

GLASHEEN, J. W. & MCMAHON, T. A. 1996 A hydrodynamic model of locomotion in the basilisk lizard. *Nature* **380**, 340–342.

GORDILLO, J. M. & GEKLE, S. 2010 Generation and breakup of Worthington jets after cavity collapse. Part 2. Tip breakup of stretched jets. *J. Fluid Mech.* **663**, 331–346.

LE GOFF, A., QUÉRÉ, D. & CLANET, C. 2013 Viscous cavities. *Phys. Fluids* **25**, 043101.

LORENCEAU, E., QUERE, D., OLLITRAULT, J. Y. & CLANET, C. 2002 Gravitational oscillations of a liquid column in a pipe. *Phys. Fluids* **14**, 1985–1992.

https://doi.org/10.1017/jfm.2014.255 Published online by Cambridge University Press

MAY, A. 1952 Vertical entry of missiles into water. *J. Appl. Phys.* **23**, 1362–1372.

MAY, A. 1975 Water entry and the cavity-running behavior of missiles. *Tech. Rep.* DTIC Document.

MEUNIER, P. & LEWEKE, T. 2003 Analysis and treatment of errors due to high velocity gradients in particle image velocimetry. *Exp. Fluids* **35**, 408–421.

MEUNIER, P. & LEWEKE, T. 2005 Elliptic instability of a co-rotating vortex pair. *J. Fluid Mech.* **533**, 125–160.

PETERS, I. R., TAGAWA, Y., OUDALOV, N., SUN, C., PROSPERETTI, A., LOHSE, D. & VAN DER MEER, D. 2013 Highly focused supersonic microjets: numerical simulations. *J. Fluid Mech.* **719**, 587–605.

SÉON, T. & ANTKOWIAK, A. 2012 Large bubble rupture sparks fast liquid jet. *Phys. Rev. Lett.* **109**, 014501.

SEYMOUR, R. S. & HETZ, S. K. 2011 The diving bell and the spider: the physical gill of *Argyroneta aquatica*. *J. Expl Biol.* **214**, 2175–2181.

TAGAWA, Y., OUDALOV, N., VISSER, C. W., PETERS, I. R., VAN DER MEER, D., SUN, C., PROSPERETTI, A. & LOHSE, D. 2012 Highly focused supersonic microjets. *Phys. Rev.* X **2**, 031002.

TAYLOR, G. 1950 The formation of a blast wave by a very intense explosion. II. The atomic explosion of 1945. *Proc. R. Soc. Lond.* A **201**, 175–186.

TRUSCOTT, T. T., BRENDEN, P. E. & BELDEN, J. 2014 Water entry of projectiles. *Annu. Rev. Fluid Mech.* **46**, 355–378.

WORTHINGTON, A. M. 1908 *A Study of Splashes*. Longmans, Green, and Co.

WORTHINGTON, A. M. & COLE, R. S. 1900 Impact with a liquid surface studied by the aid of instantaneous photography. Paper II. *Phil. Trans. R. Soc. Lond.* A **194**, 175–199.

https://doi.org/10.1017/jfm.2014.255 Published online by Cambridge University Press